Jurnal Kejuruteraan 37(5) 2025: 2505-2520
https://doi.org/10.17576/jkukm-2025-37(5)-36

Analysis of Color Features Using Machine Learning Techniques for Classification of Retinal Vessels

Assyareefah Hudaibah Saad[a], Wan Mimi Diyana Wan Zaki[a*] , Nur Asyiqin Amir Hamzah[a,d], Marizuana Mat Daud[b] & Wan Haslina Wan Abdul Halim[c]

[a]*Department of Electrical, Electronic and Systems Engineering, Faculty of Engineering and Built Environment, Universiti Kebangsaan Malaysia, Selangor, Malaysia*

[b]*Institute of Visual Informatics (IVI), Universiti Kebangsaan Malaysia (UKM), Selangor, Malaysia*

[c]*Department of Ophtalmology, Universiti Kebangsaan Malaysia Medical Centre, Kuala Lumpur, Malaysia*

[d]*Centre of Advanced Analytics, Faculty of Engineering & Technology, Multimedia University, Melaka, Malaysia*

[*]*Corresponding author: wmdiyana@ukm.edu.my*

Received 11 February 2025, Received in revised form 21 April 2025
Accepted 21 May 2025, Available online 30 August 2025

ABSTRACT

The retina, a transparent neural tissue lining the eye, is crucial for detecting both ocular and systemic diseases through imaging techniques such as fundus photography, OCT, and angiography. Recent advancements in artificial intelligence and machine learning have significantly improved retinal image analysis, enabling automated classification of arteries and veins to assists in diagnosing conditions like diabetic retinopathy, glaucoma, and systemic diseases such as hypertension and Chronic Kidney Disease (CKD). However, pixel-level analysis of retinal features, particularly colour features, remains underexplored, with challenges such as image variability and non-linear feature relationships hindering optimal classification. This study addresses these gaps by analyzing nine colour features—Red, Green, Blue, Hue, Saturation, Value, Y, Cb, and Cr—extracted pixel-wise from regions of interest (ROI) across three datasets: DRIVE, HRF, and VICAVR. A total of 3864, 9804, and 7466 normalized artery and vein pixel values underwent F-tests and two-sample T-tests, revealing statistically significant differences ($p < 0.05$) for all features. The Minimum Redundancy Maximum Relevance (mRMR) algorithm ranked features by relevance, and combinations of top-ranked features were evaluated using nine machine learning classifiers. The Ensemble model, utilizing Random Forest Bagging with Decision Tree learners and optimized hyperparameters, achieved the highest AUC scores: 91% (DRIVE), 88.2% (HRF), and 90.1% (VICAVR). Incorporating all nine features yielded the best classification results, emphasizing their complementary roles. These findings demonstrate the potential of colour features in improving retinal vascular analysis, offering insights for non-invasive diagnostics and disease monitoring.

Keywords: Artery-vein classification, colour feature, image processing, machine learning, pixel-level analysis

INTRODUCTION

The retina is an organ composed of transparent neural tissue that lines the interior of the eye, functioning as the primary receptor for visual stimuli. It is ideally suited for optical imaging to detect pathological changes (D'Amico 1994; Li et al. 2018). The uniqueness of retina has elevated the field of ophthalmology and medicine by enabling discoveries that extend beyond ocular diseases to include various systemic conditions through the use of retinal imaging. Retinal imaging plays a decisive role in visualizing the retina and optic nerve, aiding in the diagnosis of conditions such as Age-related Macular Degeneration (AMD), Retinitis Pigmentosa and Glaucoma

(Kiser & Palczewski 2016; Kotowski et al. 2014; Riazi Esfahani et al. 2023). It further identifies abnormalities in retinal blood vessels linked to systemic disorders, including cardiovascular disease, diabetes, hypertension, stroke, kidney failure and cognitive decline, highlighting its role in non-invasive diagnostics and comprehensive health evaluations (Amir Hamzah et al. 2024; Farrah et al. 2020; Pérez et al. 2012).

In capturing retinal details, imaging techniques such as fundus photography, optical coherence tomography (OCT), and angiography provide detailed insights into retinal pathologies, particularly in diabetic retinopathy and vascular diseases (Häner et al. 2023; Nanegrungsunk et al. 2022). These techniques generate high-resolution data that, when combined with advanced image processing algorithms, enable precise visualization and analysis of retinal structures. Recent advancements, including widefield imaging and artificial intelligence-assisted analysis, have significantly enhanced diagnostic precision and predictive capabilities (Häner et al. 2023). AI-assisted retinal imaging has the potential to improve screening efficiency, diagnostic accuracy, and treatment optimization, addressing the growing burden on healthcare systems due to an aging population and increasing prevalence of retinal and/or systemic diseases that can be detected from retinal images (Heger & Waldstein 2024; Sorrentino et al. 2020; Zubair et al. 2023). Additionally, image processing methods such as feature extraction, denoising, and segmentation are pivotal in refining the accuracy and efficiency of retinal image interpretation. Cutting-edge developments in artificial intelligence, particularly deep learning (DL) and machine learning, have revolutionized retinal image analysis by automating classification, diagnosis, and segmentation of retinal diseases (Li et al. 2023; Veena et al. 2022).

Deep and machine learning techniques have shown significant promise in automating retinal disease diagnosis and analysis, leveraging extensive datasets and advanced computational resources (Ali et al. 2024; Ali Malla et al. 2024; Barros et al. 2020). For diabetic retinopathy detection, integrating image preprocessing with machine learning algorithms like Weighted KNN, Cubic SVM, and Simple Tree has resulted in accuracies of 85.8-88.6% (Sharma et al. 2021). In vessel segmentation, particularly for thin vessels, the use of joint segment-level and pixel-wise loss functions has outperformed state-of-the-art methods (Yan et al. 2018). Additionally, convolutional neural networks (CNNs) trained on image patches have excelled in detecting multiple retinal lesions, such as hemorrhages, microaneurysms, and exudates, achieving pixel-wise Area Under Curve (AUC) of 0.94-0.95 and lesion-wise Area Under the Curve – Precision Recall (AUC-PR) of 0.64-0.86 (Lam et al. 2018). These advancements highlight the significance of the transformative role of machine and deep learning in retinal image analysis and disease detection.

Recent research has further highlighted the potential of machine learning in the automated classification of retinal arteries and veins at the pixel level. CNNs have achieved accuracies of 93.3% on the DRIVE database for pixel-wise classification (Girard & Cheriet 2017), while U-Net, combined with tracking algorithms, has demonstrated a vessel-wise classification accuracy of 93.57% (Li et al. 2020). Earlier neural network approaches, such as back propagation and probabilistic neural networks, attained accuracies of 83.9% and 85.1%, respectively, for pixel classification (Chhabra & Bhushan 2014). More advanced methods, integrating fundus images with fluorescein angiography using dual-input CNNs and hierarchical graph neural networks, have shown improved performance (Go et al. 2022). These developments not only enhance the classification of retinal arteries and veins but also enable the accurate assessment of the arteriovenous ratio (AVR), a critical biomarker for systemic diseases such as diabetes and hypertension.

Aside from past studies on retinal artery and vein classification, recent advancements have yet to fully explore the potential of pixel-level information, particularly by focusing solely on colour features across various datasets, for automated classification. Challenges in pixel-wise classification, such as variability in image quality and the non-linear relationships among features, continue to hinder optimal performance. Addressing these challenges could lead to improved classification accuracy and a deeper understanding of subtle variations in retinal vascular patterns.

Thus, this study aims to advance the classification of retinal arteries and veins by analysing the efficiency of nine colour features—Red, Green, Blue, Hue, Saturation, Value, Y, Cb, and Cr—extracted from specific regions of interest (ROI) within the vessels. By evaluating these features, the study employs machine learning techniques to assess the suitability of various classifiers in distinguishing between arteries and veins across three distinct datasets. The analysis of machine learning performance metrics is used to identify the most efficient features for accurately classifying retinal arteries and veins. These findings offer valuable insights into the role of colour features in non-invasive diagnostics and their potential in enhancing retinal vascular analysis for health monitoring and disease detection.

METHODOLOGY

This study builds upon previous research on vessel segmentation and identification (Ali et al. 2019, 2021; Nasiruddin et al. 2022), utilizing the Digital Retinal Images for Vessel Extraction (DRIVE) (Staal et al. 2004), which contains 20 digital fundus images (DFIs); the High-Resolution Fundus (HRF) (Budai et al. 2013), with 45 DFIs; and the VICAVR dataset (Vázquez et al. 2013), with 42 DFIs. These datasets were chosen for their well-documented ground truth annotations and their demonstrated high classification rates in prior studies.

These datasets provide a reliable basis for analysing retinal vessel characteristics essential for classification tasks. Pixels corresponding to all detected arteries and veins were extracted from the DFIs in the DRIVE, HRF, and VICAVR datasets and subsequently used to create the training dataset, providing the foundation for the feature extraction process. The feature extraction focuses on nine colour features: Red, Green, Blue, Hue, Saturation, Value, Luminance (Y), Chrominance-Blue (Cb), and Chrominance-Red (Cr). These features are analysed pixel-wise within specified regions of interest (ROIs). The selection of these ROIs was informed by previous studies (Knudtson et al. 2003; Parr & Spears 1974), that highlight their significance in capturing information relevant to systemic disease analysis.

To streamline the classification process, this study employed a feature ranking algorithm to prioritize features based on their relevance and redundancy. The ranked features are then systematically selected to identify the best-performing subsets for classification. The overall methodology, as outlined in Figure 1, encompasses several stages: pre-processing, feature extraction, statistical analysis, feature ranking and selection, and model evaluation. Classification was performed using nine types of supervised machine learning. These classifiers provide a comprehensive assessment of feature efficacy in distinguishing between retinal arteries and veins.

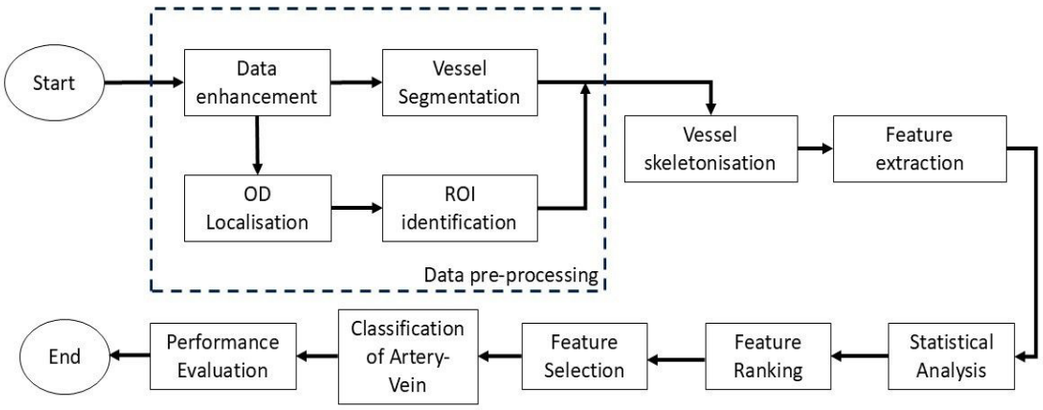

FIGURE 1. Flow chart illustrating the step-by-step process in this work.

DATA PRE-PROCESSING

In the data pre-processing phase, the contrast of retinal blood vessels was first enhanced to improve their visibility. Segmentation was then performed using a Random Forest (RF) classifier, combined with Frangi and B-COSFIRE filters, as proposed by Ali et al.(Ali et al. 2019, 2021). This procedure was essential for identifying the regions of interest (ROIs). Localization of the optical disc, which defines these ROIs, is a vital step before feature extraction, as illustrated in Figure 2(b). Afterward, skeletonization, as shown in Figure 2(c), was applied to minimize foreground pixels while preserving the connectivity of the vessels. This process effectively isolated the ROIs for further analysis, as depicted in Figure 2(d). Pixel-wise colour features were subsequently extracted from these ROIs to aid in classification. The pre-processing workflow, as depicted in Figure 2, ensured that the dataset is prepared consistently, facilitating accurate colour feature analysis.

FEATURE EXTRACTION

Feature extraction involved identifying arteries and veins from the segmented vasculature by annotating vessel skeleton coordinates within the regions of interest (ROIs). The intersection of the vessel skeleton and the ROI ring was used to determine (x, y) query points, as shown in

Figure 3(a) for binary segmented vessels and Figure 3(b) for RGB segmented vessels, with colour intensity overlaid on the ground truth to validate the classification. Circular masks were then applied to create smaller ROIs around these points, as depicted in Figure 3(c), allowing for pixel-wise extraction of colour features. The nine colour features were systematically recorded to provide a thorough characterization. Figure 3(d) shows the coordinates overlaid on the RGB retinal fundus image for colour feature extraction, while Figure 3(e) provides a close-up view of the process. This method ensured the accuracy of the data for artery-vein classification. The step-by-step procedure is summarized in Figure 3, which illustrates the process for obtaining the ROIs.

STATISTICAL VALIDATION OF FEATURE DISCRIMINATIVE POWER

Statistical tests were conducted to validate the discriminative power of pixel-level colour features in distinguishing arteries from veins, across multiple datasets. This validation ensured the selected features genuinely contributed to the classification task. The F-test and two-sample t-test were employed as complementary statistical tools.

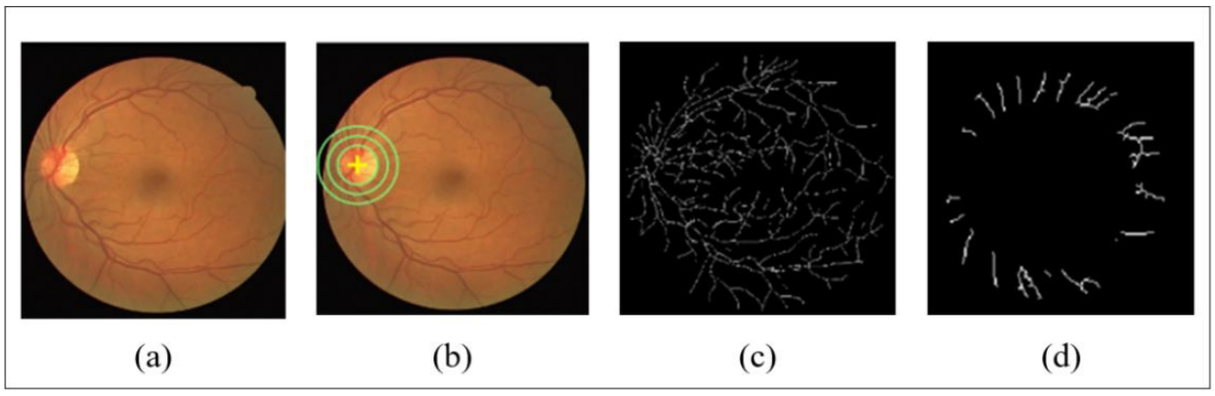

FIGURE 2. Data Processing workflow. (a) Original retinal fundus image; (b) Identified ROI using localised optical disk; (c) Skeletonized vessels; (e) Skeletonized vessels within the ROIs.

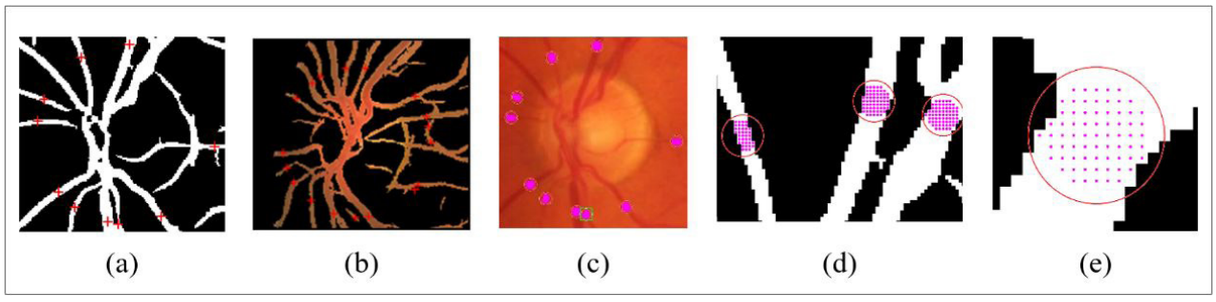

FIGURE 3. Procedural steps for colour feature extraction. (a) & (b) Identified *(x,y)* coordinates in the ROIs for binary and RGB segmented vessels; (c) Annotated *(x,y)* coordinates on RGB retinal fundus image for colour feature extraction; (d) & (e) A close-up view of selected pixels on binary segmented vessels.

The F-test compared the variances of the artery and vein groups for each feature. A p-value greater than 0.05 indicated no significant variance differences, allowing for a two-sample t-test assuming equal variances. Conversely, features with p-values less than 0.05 were analyzed using Welch's t-test, as it accounts for unequal variances. This systematic approach ensured the appropriate statistical method was applied to each feature. The formula for the F-test is given as:

$$F = \frac{s_1^2}{s_2^2} \quad (1)$$

Where s_1^2 and s_2^2 represent the variances of the artery and vein groups, respectively.

The two-sample t-test assessed mean differences between artery and vein groups for each feature, accounting

for variability across datasets. This robust analysis ensured that the selected features genuinely contributed to the classification task. Formula below shows the two-sample T-test formula:

$$T = \frac{\bar{X}_1 - \bar{X}_2}{\sqrt{\frac{s_1^2}{n_1} + \frac{s_2^2}{n_2}}} \quad (2)$$

Where $\bar{X}_1$ and $\bar{X}_2$ are the means of the artery and vein groups, s_1^2 and s_2^2 are the variances of the two groups, and n_1 and n_2 are the sample sizes of the artery and vein groups, respectively. This statistical analysis ensured rigorous evaluation, with results detailed in the Results and Discussion section.

FEATURE RANKING

Feature ranking serves as a preliminary step in evaluating the importance of individual features for classification tasks. This study employed the Minimum Redundancy Maximum Relevance (mRMR) algorithm, a widely used filter-based method, to rank the nine colour features (Red, Green, Blue, Hue, Saturation, Value, Y, Cb, and Cr). This selection was motivated by the close similarity in the values of colour features between arteries and veins, which will be discussed in the result and discussion section.

The mRMR algorithm was chosen for its ability to balance two crucial aspects: maximizing relevance to the target variable while minimizing redundancy among features. This dual criterion ensured that the ranked features not only contribute significantly to the classification task but also avoid overlapping information, thereby enhancing the interpretability and efficiency of machine learning models. By using statistical measures such as mutual information, mRMR quantifies relevance and redundancy, allowing features with high relevance (strong association with classification labels) and low redundancy (unique contributions) to be prioritized.

The mRMR algorithm aims to identify the best set of features, denoted as S, that maximizes V_s, the relevance of S with respect to a response variable y, while minimizing W_s, the redundancy within S. These are defined as:

$$V_S = \frac{1}{|S|} \sum_{x \in S} I(x, y), \quad (3)$$

$$W_S = \frac{1}{|S|^2} \sum_{x,z \in S} I(x, z), \quad (4)$$

Where, $|S|$ is the number of features in S, $I(x,y)$ measures the dependency between feature x and the response variable y, and $I(x,z)$ quantifies the redundancy between features x and z.

For instance, in the context of retinal vessel classification, some features might capture pigmentation contrasts or highlight subtle structural differences. The ranking process provided valuable insights into the individual contributions of each feature, guiding subsequent decisions on their inclusion in the classification pipeline.

FEATURE MODEL AND SELECTION

All nine features were analysed and selected based on their performance in classifying arteries and veins, starting from the top-ranked to the lowest-ranked features, as determined by the feature ranking algorithm. This step evaluated each feature's contribution to classification and identifies the most effective machine learning classifier for artery and vein classification.

The selected supervised machine learning classifiers include Decision Tree, Discriminant Analysis, Naïve Bayes, Support Vector Machine (SVM), Linear Classifiers, Nearest Neighbor, Kernel Approximation, Ensemble, and Neural Network. These classifiers represent both parametric and non-parametric models and were compared to assess their effectiveness. A standard 5-fold cross-validation was applied to all models to avoid overfitting and improve generalization. In each fold, 80% of the data served as training data while the remaining 20% was used for testing, for every dataset.

The decision to include all nine features, despite their ranking, was based on the goal of maximizing classifier performance. Retaining the full feature set ensures that no potentially valuable information is excluded, given the complexity of retinal vascular structures. Additionally, preserving all features helps capture potential interactions between features that could provide unique insights when combined.

Feature selection was employed to optimize the use of available data while balancing computational efficiency with comprehensive analysis. The selected features were then evaluated using nine supervised machine learning classifiers, suited to a manually labeled dataset. The objective is to identify the model that delivers the best results in classifying arteries and veins. Next, model performance was assessed using several evaluation metrics, including the AUC, Accuracy, Sensitivity, and Specificity for a comprehensive evaluation. AUC was computed using the trapezoidal rule, as shown below:

$$\boldsymbol{AUC} = \sum_{i=1}^{n-1}(FPR_{i+1} - FPR_i) \cdot \frac{TPR_{i+1}+TPR_i}{2} \quad (5)$$

where TPR is the true positive rate and FPR is the false positive rate at different thresholds.

The remaining metrics are defined as follows:

$$\boldsymbol{Accuracy} = \frac{TP+TN}{TP+FP+TN+FN} \quad (6)$$

$$\boldsymbol{Sensitivity} = \frac{TP}{TP+FN} \quad (7)$$

$$\boldsymbol{Specificity} = \frac{TN}{TN+FP} \quad (8)$$

where Tp is true positive, TN is true negative, FP is false positive, and FN is false negative.

RESULTS AND DISCUSSION

A total of 3864, 9804, and 7466 normalised and balanced artery and vein pixel values were extracted from the DRIVE (20 images), HRF (45 images), and VICAVR (42 images) datasets, respectively. These pixel values form the foundation for identifying optimal colour features.

There is a noticeable similarity in the colour feature values between arteries and veins, likely due to factors such as the natural lighter hue of arteries and imaging conditions. Arteries, typically lighter with a reddish-orange hue, may resemble the lighter portions of veins. Additionally, the lighting and imaging process can influence how the colours of both vessels are captured. While veins are generally darker, subtle similarities can arise from variations in vessel thickness and lighting conditions. Table 1 shows the colour feature values for retinal arteries and veins across selected images

In the DRIVE dataset, arteries and veins show subtle differences across features. For Image 01_test, arteries have slightly higher Red, Green, and Blue values than veins, with differences of 0.003921, 0.031372, and 0.02353, respectively. Similar small variations are seen in Saturation (0.03237) and Value (0.003921). The Y, Cb, and Cr features differ by 0.019127, 0.000624, and 0.011496, respectively. This trend continues in Image 09_test and Image 017_test, where Red values show minimal differences (~0.00392), while Green and Blue exhibit larger variations. Saturation and Value remain consistent, with minor variations in Y, Cb, and Cr. Overall, Red shows the smallest differences, while Green, Blue, and Saturation exhibit slightly greater variability.

In the HRF dataset, feature differences are more pronounced. For Image 01_h, arteries and veins differ significantly in Green (0.113725) and Blue (0.027451) values, while Red shows a minimal difference of 0.003922. Saturation and Y exhibit notable variations of 0.034761 and 0.061027, respectively. Similar trends are observed in Image 06_dr and Image 09_g, where Green and Blue dominate the differences, while Red remains largely consistent. Saturation and Y also vary noticeably, whereas Hue, Cb, and Cr are more stable. Across the dataset, Green, Blue, and Saturation are the most distinguishing features.

In the VICAVR dataset, the differences are subtler. For Image 27, Red values are identical for arteries and veins, while Green and Blue differ slightly (0.015686 and 0.019608). Small variations are also seen in Saturation (0.023148) and Y (0.005988). Similar patterns occur in Image 41 and Image 55, where Red remains consistent, while Green and Blue show slight differences. Saturation and Y exhibit minor variations, and Cb and Cr are mostly identical. Overall, the VICAVR dataset shows smaller differences across all features, with Green, Blue, and Saturation providing the most distinction.

Across the randomly selected images in DRIVE, HRF, and VICAVR datasets, Red values generally show minimal differences between artery and vein, with some images exhibiting identical Red values. Green and Blue values tend to have larger variations, especially in certain images, while Hue differences are usually small. Saturation and Value differences vary but are typically subtle across the datasets. Y values show slight differences, and Cb and Cr values remain mostly consistent between artery and vein, with occasional minor variations. Overall, the datasets exhibit subtle to moderate differences in features.

STATISTICAL ANALYSES AND VALIDATION OF FEATURE DISCRIMINATION ABILITY

Thus, before proceeding to feature ranking, F-test and two sample t-test statistical analyses were conducted to validate the discriminative ability of the features. This step was crucial to ensure that all features could effectively distinguish between arteries and veins. Any feature lacking this ability would be excluded prior to applying the feature ranking algorithm.

TABLE 1. Colour features values for retinal arteries and veins across randomly selected images.

Dataset	Images	Vessel	Red	Green	Blue	**Hue**	**Saturation**	**Value**	**Y**	**Cb**	**Cr**
DRIVE	01_test	Artery	0.690196	0.443137	0.231373	0.076923	0.664773	0.690196	0.486031	0.37233	0.625599
		Vein	0.686275	0.411765	0.207843	0.071038	0.697143	0.686275	0.466904	0.371706	0.637095
	09_test	Artery	0.776471	0.466667	0.247059	0.069136	0.681818	0.776471	0.521583	0.359585	0.653718
		Vein	0.772549	0.407843	0.235294	0.053528	0.695431	0.772549	0.489769	0.372117	0.674470
	017_ test	Artery	0.643137	0.443137	0.258824	0.079932	0.597561	0.643137	0.476634	0.391363	0.602969
		Vein	0.639216	0.392157	0.231373	0.065705	0.638037	0.639216	0.447239	0.394722	0.621957
HRF	01_h	Artery	0.764706	0.368627	0.196078	0.050575	0.743590	0.764706	0.464146	0.367466	0.688249
		Vein	0.760784	0.254902	0.168627	0.024283	0.778351	0.760784	0.403119	0.389084	0.730315
	06_dr	Artery	0.843137	0.231373	0.145098	0.020599	0.827907	0.843137	0.410100	0.373390	0.776820
		Vein	0.847059	0.188235	0.188235	0.000000	0.777778	0.847059	0.393584	0.404308	0.791326
	09_g	Artery	0.607843	0.215686	0.082353	0.042289	0.864516	0.607843	0.335629	0.385272	0.683726
		Vein	0.603922	0.211765	0.078431	0.042289	0.870130	0.603922	0.332261	0.385272	0.683726
VICAVR	27	Artery	0.847059	0.474510	0.145098	0.078212	0.828704	0.847059	0.533680	0.302057	0.689119
		Vein	0.847059	0.490196	0.125490	0.084239	0.851852	0.847059	0.539668	0.288881	0.684751
	41	Artery	0.760784	0.325490	0.003922	0.070812	0.994845	0.760784	0.422579	0.296202	0.716118
		Vein	0.760784	0.298039	0.054902	0.057407	0.927835	0.760784	0.413731	0.326581	0.722572
	55	Artery	0.737255	0.274510	0.078431	0.049603	0.893617	0.737255	0.398131	0.347250	0.719211
		Vein	0.733333	0.270588	0.074510	0.049603	0.898396	0.733333	0.394763	0.347250	0.719211

The F-test was included due to the diverse nature of the colour feature data, which were extracted from numerous vessels across different images within each dataset. This approach emphasizes the independence of the data, as the colour feature measurements (Red, Green, Blue, Hue, Saturation, Value, Y, Cb, and Cr) were derived from multiple retinal vessels (arteries and veins) spanning several images in a single dataset.

A two-sample t-test was selected for this analysis. However, determining whether the data exhibit equal or unequal variances is a prerequisite. This necessitated the use of the F-test for equality of variances to compare the variances of the artery and vein classes. If the F-test indicates no significant difference in variances (p-value > 0.05), the feature is assumed to have equal variances between the two classes, and the two-sample t-test assuming equal variances is applied. Conversely, if the F-test reveals a significant difference in variances (p-value < 0.05), Welch's t-test is utilized, as it accounts for unequal variances. The results of the F-test and two sample t-test performed on each feature across all datasets are presented in Table 2.

Based on Table 2, it can be observed that the features Y and Cr in both the DRIVE and HRF datasets exhibit equal variances, as indicated by F-test p-values > 0.05. Similarly, in the VICAVR dataset, Saturation also demonstrates equal variances. However, when a two-sample t-test assuming equal variances (pooled t-test) was conducted for these features, all were found to be significantly different between the two classes, with p-values < 0.05. This indicates that these features reject the null hypothesis of no significant difference in means between the two groups, despite having similar variances.

For the remaining features in all datasets, the F-test revealed unequal variances (p-value < 0.05), necessitating the use of Welch's t-test. Welch's t-test results confirmed that all these features were also significantly different between arteries and veins, with p-values below 0.05.

In conclusion, the statistical analysis validates that all tested features exhibit significant differences in either variances or means, making them viable candidates for feature ranking. The results confirm that these colour features possess discriminative ability, enabling them to effectively distinguish between artery and vein classes. This ensures the features are robust and reliable inputs for classification models, as they provide meaningful distinctions crucial for accurate categorization.

By confirming the statistical significance of the features, this step lays the foundation for their prioritization using feature ranking algorithms. Subsequently, the ranked features can guide the development of optimized classification models, improving their predictive performance and ensuring accurate differentiation between arteries and veins.

TABLE 2. Statistical analysis results of colour features using F-test and Two Sample t-test across DRIVE, HRF, and VICAVR datasets.

Dataset	Feature	F-test p-value	T-test t-statistic	T-test p-value	T-test Type	Significance
DRIVE	Red	3.60×10^{-3}	11.20	1.14×10^{-8}	UV	Yes
	Green	5.60×10^{-3}	12.46	5.45×10^{-35}	UV	Yes
	Blue	6.72×10^{-7}	6.23	5.13×10^{-10}	UV	Yes
	Hue	<0.0001	2.00	4.57×10^{-2}	UV	Yes
	Saturation	2.05×10^{-8}	3.23	1.03×10^{-3}	UV	Yes
	Value	3.60×10^{-3}	11.20	1.14×10^{-28}	UV	Yes
	Y	1.39×10^{-1}	13.20	5.87×10^{-39}	EV	Yes
	Cb	3.00×10^{-4}	-13.63	2.56×10^{-41}	UV	Yes
	Cr	2.89×10^{-1}	6.79	1.30×10^{-11}	EV	Yes
HRF	Red	2.94×10^{-2}	21.60	4.40×10^{-101}	UV	Yes
	Green	2.36×10^{-5}	37.11	3.60×10^{-282}	UV	Yes
	Blue	1.4×10^{-3}	20.65	9.71×10^{-93}	UV	Yes
	Hue	<0.0001	4.99	6.16×10^{-7}	UV	Yes
	Saturation	4.0×10^{-4}	-14.98	3.64×10^{-50}	UV	Yes
	Value	2.94×10^{-2}	21.60	4.40×10^{-101}	UV	Yes
	Y	4.25×10^{-1}	33.05	3.60×10^{-227}	EV	Yes
	Cb	9.7×10^{-3}	-30.63	7.20×10^{-197}	UV	Yes
		6.94×10^{-2}	2.40	1.65×10^{-2}	EV	Yes

continue ...

... cont.

VICAVR	Red	<0.0001	9.86	9.09×10^{-23}	UV	Yes
	Green	6.23×10^{-19}	42.55	<0.0001	UV	Yes
	Blue	7.34×10^{-9}	9.49	3.05×10^{-21}	UV	Yes
	Hue	1.28×10^{-10}	41.46	<0.0001	UV	Yes
	Saturation	9.2×10^{-2}	-6.97	3.50×10^{-12}	EV	Yes
	Value	<0.0001	9.86	9.09×10^{-23}	UV	Yes
	Y	1.10×10^{-3}	35.15	1.40×10^{-250}	UV	Yes
	Cb	2.95×10^{-2}	-27.22	1.10×10^{-155}	UV	Yes
	Cr	3.89×10^{-15}	-24.19	2.10×10^{-124}	UV	Yes

FEATURE RANKING

The validated features were then subjected to the mRMR algorithm for ranking. By ensuring that only statistically significant features were considered, the integration of F-tests and two sample t-tests enhanced the reliability of the feature ranking process. This dual-layered approach provided a robust foundation for identifying the most effective features for artery and vein classification.

Figure 4 demonstrates the ranking of colour features across three datasets, DRIVE, HRF, and VICAVR, using the mRMR algorithm. The mRMR algorithm helps identify the most relevant features while minimizing redundancy between them, making it useful for feature selection in machine learning classification later. mRMR is particularly valuable when working with large datasets, as it helps reduce dimensionality by prioritizing features that offer the most information with minimal overlap.

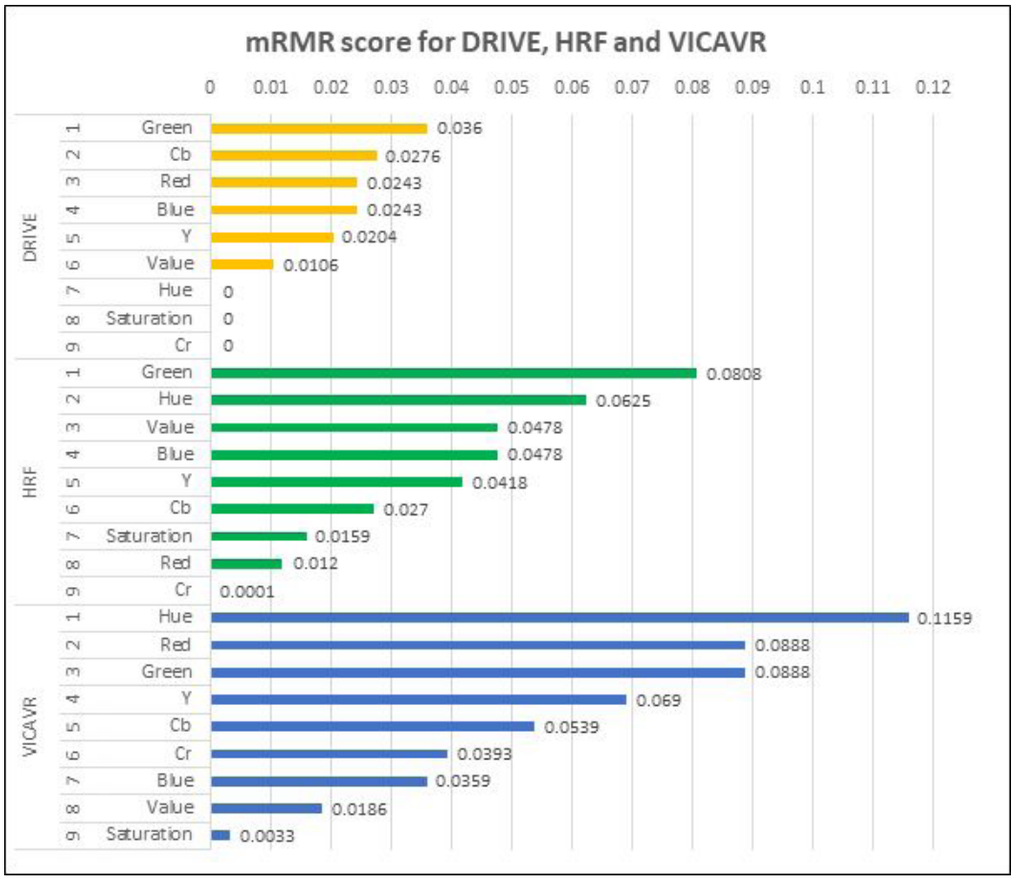

FIGURE 4. Feature ranking using mRMR across all datasets.

In the DRIVE dataset, Green ranks first with the highest mRMR score of 0.036, followed by Cb and Red with scores of 0.0276 and 0.0243, respectively. Features such as Hue, Saturation, and Cr are ranked lowest with scores of 0, indicating their minimal relevance. These results suggest that, in the DRIVE dataset, certain colour features like Green and Cb have a higher impact on the analysis compared to others, guiding future feature selection in this dataset.

In the HRF dataset, Green ranks highest with a score of 0.0808, followed by Hue at 0.0625 and Value at 0.0478. This shows that features like Hue and Value are more relevant in this dataset compared to the DRIVE dataset. On the other hand, Cr has a very low score of 0.0001, suggesting that it is nearly irrelevant in the HRF dataset. These variations across datasets highlight the importance of understanding feature relevance within the specific context of each dataset being analyzed.

In the VICAVR dataset, Hue takes the top spot with a score of 0.1159, followed by Red and Green with scores of 0.0888. These features are shown to be the most significant in this dataset. However, Saturation ranks last with a score of 0.0033, indicating its minimal contribution to the analysis. This reinforces the need for dataset-specific feature selection to prioritize the most informative features.

These varying rankings highlight the dataset-specific relevance of certain features, which can significantly impact model performance and computational efficiency. By applying the mRMR algorithm, we can efficiently select the most relevant and non-redundant features, ensuring that only the most informative data is used for further analysis or modeling.

FEATURE AND MODEL SELECTION

While feature ranking identified the relative importance of each colour feature, the inclusion of the top-ranked features, from top 1 to top 9, in the classification process was guided by experimental findings. Retaining the complete set of features ensured that no potentially valuable information was omitted. This comprehensive approach facilitated a robust evaluation of how different classifiers utilized the richness of the data and the interactions among features.

The inclusion of all ranked features also mitigated potential limitations associated with ranking-based methods. Although mRMR prioritized the most relevant features, excluding lower-ranked features could inadvertently disregard those that contribute indirectly to classification performance. For example, certain colour features may exhibit synergistic interactions, yielding unique insights when consider collectively rather than in isolation. By preserving the entire range of features, this study sought to maximize the classifiers' capacity to discern subtle variations in retinal artery and vein characteristics.

Table 3 presents the best performance metrics achieved by each classifier model conducted with 5-fold cross-validation, evaluated on the top 1 to top 9 ranked features across all datasets. Table 4 complements these results by detailing the optimized hyperparameters fine-tuned to achieve the metrics outlined in Table 3. The hyperparameter configurations provide a clear summary of the parameters contributing to the optimal performance of each model, facilitating reproducibility and a deeper understanding of the training process.

The Ensemble model demonstrates the highest AUC scores across all datasets, achieving 91%, 88.2%, and 90.1% for DRIVE, HRF, and VICAVR, respectively. These AUC values indicate the model's excellent classification capability, effectively classify between artery and vein classes while minimizing false positives and false negatives.

These results highlight the model's robustness in capturing the complex features of retinal vessels. Notably, the highest performance is achieved when all nine features are included, suggesting that, despite some redundancy identified in the mRMR analysis, each feature contributes valuable information. All colour features, play a crucial role in accurately classifying artery and vein vessels. Even with some overlap, each feature provides essential insights that enhance the model's performance. The inclusion of all nine features enables the model to leverage subtle interactions, further improving its classification ability.

The varying importance of the colour features across datasets can be attributed to both biological structures and imaging characteristics. For instance, the Green channel is particularly effective in enhancing vessel visibility and structural contrast in retinal images. It highlights subretinal masses, retinal vessels, and layers, making it one of the most reliable channels for detecting abnormalities in non-neural network-based systems (Biswas et al. 2022). On the other hand, the Red channel is useful for visualizing choroidal details but is more susceptible to interference from subretinal blood, which blocks red light and affects visibility in deeper layers. Meanwhile, the Blue channel enhances the visibility of the nerve fiber layer but provides less contrast for vessel segmentation compared to green(Marco A. Zarbin 2012).

Features in the Hue, Saturation and Value color space also contribute significantly. Hue and Saturation components are particularly valuable in addressing uneven illumination and low contrast—two common issues in retinal imaging. Accurate hue representation has been

linked to improved diagnostic accuracy and enhanced detection of pathological features (Sarao et al. 2019). Moreover, the separation of luminance and chromaticity in Hue, Saturation and Value allows for more precise illumination correction without introducing artifacts (Grisan et al. n.d.; Zhao et al. 2023; Zhou et al. 2018).

The Cb component from the YCbCr color space plays a complementary role. This feature is especially effective under low-light conditions or in non-uniform lighting environments, helping to recover important image details and enabling more accurate pixel classification (Anzueto-Rios et al. 2017; Yang & Qin 2023).

Meanwhile, the consistent high performance of the Ensemble model is attributed to the Bagging method, specifically employing Random Forest with tree learners as the optimized hyperparameter. This method reduces overfitting by combining the predictions from multiple decision trees inside Random Forest, each trained on a different portion of the data. To ensure generalizability, all models underwent 5-fold cross-validation.

In contrast, the SVM model achieves the highest accuracy and specificity in the DRIVE dataset, with scores of 83.2% and 86.4%, respectively. This suggests that SVM is particularly effective in distinguishing between arteries and veins, minimizing false positives. In the HRF dataset, the SVM and Nearest Neighbour models exhibit higher sensitivity, with scores of 81.2% and 82.5%, respectively, compared to the Ensemble model's sensitivity of 81.1%. This indicates that SVM and Nearest Neighbour are slightly better at identifying true positives, which is critical for applications requiring high detection of rare events. However, in the VICAVR dataset, the Ensemble model outperforms all others across all metrics, demonstrating superior generalization and robustness in handling the dataset's complexity. This consistent top performance in the VICAVR dataset underscores the Ensemble model's ability to synthesize the strengths of multiple decision trees, achieving enhanced accuracy, sensitivity, and specificity, with an AUC of 90.1%, accuracy of 82.4%, sensitivity of 83.7%, and specificity of 81.4%.

Furthermore, performance metrics presented in Table 3 highlights that non-parametric machine learning models consistently outperform other models. Unlike parametric models, which rely on predefined assumptions about data distribution and structure, non-parametric models like the Ensemble and Nearest Neighbour are inherently flexible. This flexibility allows them to handle complex, high-dimensional data with intricate relationships, such as those exhibited by retinal vessel characteristics. As a result, non-parametric models excel in identifying subtle patterns within the data, leading to superior classification outcomes. These findings suggest that non-parametric models, particularly ensemble classifiers, are not only effective but also generalizable for pixel-wise medical imaging tasks, making them well-suited for similar applications.

TABLE 3. Classification results: best performance metric (AUC, Accuracy, Sensitivity, Specificity) for each classifier model across DRIVE, HRF and VICAVR.

Dataset	Model	Top	Features	AUC (%)	Accuracy (%)	Sensitivity (%)	Specificity (%)
DRIVE	Decision Tree	3	Green, Cb, Red	82.1	77.1	78.9	76.0
	Discriminant Analysis	2	Green, Cb	63.8	60.7	54.2	67.2
	Naïve Bayes	8	Green, Cb, Red, Blue, Y, Value, Hue, Saturation	70.7	63.6	61.7	65.5
	SVM	9	Green, Cb, Red, Blue, Y, Value, Hue, Saturation, Cr	89.8	83.2	86.4	79.9
	Linear Regression	6	Green, Cb, Red, Blue, Y, Value	63.2	60.4	55.6	65.1
	Nearest Neighbour	9	Green, Cb, Red, Blue, Y, Value, Hue, Saturation, Cr	88.5	82.0	85.4	78.6
	Kernel Approximation	9	Green, Cb, Red, Blue, Y, Value, Hue, Saturation, Cr	87.1	80.0	82.9	77.1
	Ensemble	9	Green, Cb, Red, Blue, Y, Value, Hue, Saturation, Cr	91.0	82.6	84.3	80.9
	Neural Network	8	Green, Cb, Red, Blue, Y, Value, Hue, Saturation	88.8	80.4	82.9	77.9

continue ...

... cont.

HRF	Decision Tree	8	Green, Hue, Value, Blue, Y, Cb, Saturation, Red	81.8	76.4	77.1	75.7
	Discriminant Analysis	4	Green, Hue, Value, Blue	72.2	66.8	63.7	69.9
	Naïve Bayes	3	Green, Hue, Value	74.4	68.3	70.3	66.4
	SVM	6	Green, Hue, Value, Blue, Y, Cb	86.4	79.7	81.2	78.2
	Linear Regression	4	Green, Hue, Value, Blue	72.1	67.2	65.5	69.0
	Nearest Neighbour	9	Green, Hue, Value, Blue, Y, Cb, Saturation, Red, Cr	84.4	79.0	82.5	75.6
	Kernel Approximation	9	Green, Hue, Value, Blue, Y, Cb, Saturation, Red, Cr	80.9	73.9	76.3	71.6
	Ensemble	9	Green, Hue, Value, Blue, Y, Cb, Saturation, Red, Cr	88.2	80.0	81.1	79.0
	Neural Network	9	Green, Hue, Value, Blue, Y, Cb, Saturation, Red, Cr	87.7	79.0	80.0	77.9
VICAVR	Decision Tree	7	Hue, Red, Green, Y, Cb, Cr, Blue	83.4	78.0	77.1	79.0
	Discriminant Analysis	3	Hue, Red, Green	77.2	68.8	65.0	72.6
	Naïve Bayes	6	Hue, Red, Green, Y, Cb, Cr	78.5	70.1	71.4	68.7
	SVM	9	Hue, Red, Green, Y, Cb, Cr, Blue, Value, Saturation	87.8	81.3	82.4	80.3
	Linear Regression	7	Hue, Red, Green, Y, Cb, Cr, Blue	77.3	69.0	66.1	71.9
	Nearest Neighbour	8	Hue, Red, Green, Y, Cb, Cr, Blue, Value	87.7	81.4	82.9	79.8
	Kernel Approximation	9	Hue, Red, Green, Y, Cb, Cr, Blue, Value, Saturation	82.0	75.6	77.8	73.4
	Ensemble	9	Hue, Red, Green, Y, Cb, Cr, Blue, Value, Saturation	90.1	82.4	83.7	81.4
	Neural Network	5	Hue, Red, Green, Y, Cb	89.5	80.8	82.0	79.8

TABLE 4. Optimized hyperparameters for classifiers models achieving best performance metrics.

Dataset	Model	Model hyperparameter
DRIVE	Decision Tree	Max no of split: 1659, Split criterion:Gini's Diversity index
	Discriminant Analysis	Discriminant type: Quadratic
	Naïve Bayes	Distribution names: Kernel Kernel Type: Gaussian
	SVM	Kernel function: Gaussian Kernel scale: 0.031389 Box constraint level: 1.3453
	Linear Regression	Learner: SVM Regularization: Lasso
	Nearest Neighbour	No of neighbors: 9 Distance metriic: Euclidean Distance weight: Squared inverse
	Kernel Approximation	Learner: SVM No of expansion dimenasions: 6932 Regularization strength: 5.7036e-07 Kernel scale:0.44392

continue ...

... cont.

	Ensemble	Ensemble method: Bag Max no of split: 3225 No of learners:489
	Neural Network	No. of fully connected layer: 1 Activation: Sigmoid Regularization strength (Lambda): 3.0311e-09 Layers: 53
HRF	Decision Tree	Max no of splits: 750 Split criterion: Max deviance reduction
	Discriminant Analysis	Discriminant Type: Linear
	Naïve Bayes	Distribution name: Kernel Kernel Type: Gaussian
	SVM	Kernel function: Gaussian Kernel scale: 0.018488 Box constraint level: 3.7005
	Linear Regression	Learner: Logistic regression Regularization: Lasso
	Nearest Neighbour	Number of neighbors: 9 Distance metric: Minkowski (cubic) Distance weight:Inverse
	Kernel Approximation	Learner: SVM No. of expansion dimensions:790 Regularization (strength): 4.6854E-05 Kernel scale: 0.006188
	Ensemble	Ensemble method: Bag Max no of splits: 3450 No of learners: 70
	Neural Network	No of fully connected layer: 2 Activation: ReLU Regularization strength (Lambda):1.909e-06 Layer: 294, 290
VICAVR	Decision Tree	Max no of splits:442 Split criterion: Max deviance reduction
	Discriminant Analysis	Discriminant type: Linear
	Naïve Bayes	Distribution names: Kernel Kernel type: Gaussian
	SVM	Kernel function: Gaussian Kernel scale: 0.04189 Box constraint level: 5.8731
	Linear Regression	Learner: SVM Regularization: Lasso
	Nearest Neighbour	No of neighbors: 45 Distance metric: Euclidean Distance weight: Squared inverse
	Kernel Approximation	Learner: SVM No. of expansion dimension: 8956 Regularization strength (Lambda):0.0069301 Kernel scale:0.0022586
	Ensemble	Ensemble method: Bag Max no of splits: 7353 No of learners: 487

CONCLUSION

The Ensemble model, employing Random Forest Bagging with Decision Tree learners, consistently outperformed other classifiers across the DRIVE, HRF, and VICAVR datasets. The model achieved AUC values of 91%, 88.2%, and 90.1% for the DRIVE, HRF, and VICAVR datasets, respectively. These results emphasize the model's effectiveness in distinguishing between artery and vein classes, showcasing its robust discriminative ability. This study focused on optimizing feature selection through meticulous ranking of colour features. While some redundancy was present, the inclusion of all features, particularly colour features, enhanced classification accuracy by capturing subtle distinctions between the classes. Although the findings are promising, future work could explore expanding the datasets and incorporating additional features to further improve classification performance, may by using hybrid AI models. Overall, the Ensemble model demonstrates strong potential for advancing automated retinal vessel classification, with significant implications for medical imaging applications.

ACKNOWLEDGEMENT

This work was supported in part by the research university grants from Universiti Kebangsaan Malaysia with Grant no. GUP-2022-005.

DECLARATION OF COMPETING INTEREST

None.

REFERENCES

Ali, A., Mimi Diyana Wan Zaki, W., Hussain, A., Haslina Wan Abdul Halim, W., Hashim, N. & Noorshahida Mohd Isa, W. 2021. B-COSFIRE and Background Normalisation for Efficient Segmentation of Retinal Vessels. *2021 IEEE Symposium on Industrial Electronics & Applications (ISIEA)*, pp. 1–5.

Ali, A., Zaki, W.M.D.W. & Hussain, A. 2019. Retinal blood vessel segmentation from retinal image using B-COSFIRE and adaptive thresholding. *Indonesian Journal of Electrical Engineering and Computer Science* 13(3): 1199–1207.

Ali Malla, M., Al-Beak, O.H., Hameed, D.M., Mohamedsheet Al-Hatab, M.M., Omar Al-Nima, R.R., Jarjees, M.S. & A. K. Al-Maqsood, K. 2024. Adopting Machine Learning to Automatically Identify a Suitable Surgery Type for Refractive Error Patients. *Jurnal Kejuruteraan* 36(4): 1749–1757.

Ali, M.A.M., Md Tahir, N. & Al-Rawe, I. 2024. File Encryption by Iris Recognition System. *Jurnal Kejuruteraan* 36(5): 1955–1963.

Amir Hamzah, N.A., Wan Zaki, W.M.D., Wan Abdul Halim, W.H., Mustafar, R. & Saad, A.H. 2024. Evaluating the potential of retinal photography in chronic kidney disease detection: a review. *PeerJ* 12: e17786.

Anzueto-Rios, A., Moreno-Cadenas, J.A., Gómez-Castañeda, F. & Garduza-Gonzalez, S. 2017. Image Segmentation Using Fuzzy Inference System on YCbCr Color Model. *Advances in Science, Technology and Engineering Systems Journal* 2(3): 460–468.

Barros, D.M.S., Moura, J.C.C., Freire, C.R., Taleb, A.C., Valentim, R.A.M. & Morais, P.S.G. 2020. Machine learning applied to retinal image processing for glaucoma detection: review and perspective. *BioMedical Engineering OnLine* 19(1): 20.

Biswas, S., Khan, Md.I.A., Hossain, Md.T., Biswas, A., Nakai, T. & Rohdin, J. 2022. Which Color Channel Is Better for Diagnosing Retinal Diseases Automatically in Color Fundus Photographs? *Life* 12(7): 973.

Budai, A., Bock, R., Maier, A., Hornegger, J. & Michelson, G. 2013. Robust Vessel Segmentation in Fundus Images. *International Journal of Biomedical Imaging* 2013: 1–11.

Chhabra, S. & Bhushan, B. 2014. Supervised pixel classification into arteries and veins of retinal images. *2014 Innovative Applications of Computational Intelligence on Power, Energy and Controls with their impact on Humanity (CIPECH)*, pp. 59–62.

D'Amico, D.J. 1994. Diseases of the Retina. *New England Journal of Medicine* 331(2): 95–106.

Farrah, T.E., Dhillon, B., Keane, P.A., Webb, D.J. & Dhaun, N. 2020. The eye, the kidney, and cardiovascular disease: old concepts, better tools, and new horizons. *Kidney International* 98(2): 323–342.

Girard, F. & Cheriet, F. 2017. Artery/vein classification in fundus images using CNN and likelihood score propagation. *2017 IEEE Global Conference on Signal and Information Processing (GlobalSIP)*, pp. 720–724.

Go, S., Kim, J., Noh, K.J., Park, S.J. & Lee, S. 2022. Combined Deep Learning of Fundus Images and Fluorescein Angiography for Retinal Artery/Vein Classification. *IEEE Access* 10: 70688–70698.

Grisan, E., Giani, A., Ceseracciu, E. & Ruggeri, A. (n.d.). Model-Based Illumination Correction in Retinal Images. *3rd IEEE International Symposium on Biomedical Imaging: Macro to Nano, 2006.*, pp. 984–987.

Häner, N.U., Dysli, C. & Munk, M.R. 2023. Imaging in retinal vascular disease: A review. *Clinical & Experimental Ophthalmology* 51(3): 217–228.

Heger, K.A. & Waldstein, S.M. 2024. Artificial intelligence in retinal imaging: current status and future prospects. *Expert Review of Medical Devices* 21(1–2): 73–89.

Kiser, P.D. & Palczewski, K. 2016. Retinoids and Retinal Diseases. *Annual Review of Vision Science* 2(1): 197–234.

Knudtson, M.D., Lee, K.E., Hubbard, L.D., Wong, T.Y., Klein, R. & Klein, B.E.K. 2003. Revised formulas for summarizing retinal vessel diameters. *Current Eye Research* 27(3): 143–149.

Kotowski, J., Wollstein, G., Ishikawa, H. & Schuman, J.S. 2014. Imaging of the optic nerve and retinal nerve fiber layer: An essential part of glaucoma diagnosis and monitoring. *Survey of Ophthalmology* 59(4): 458–467.

Lam, C., Yu, C., Huang, L. & Rubin, D. 2018. Retinal Lesion Detection With Deep Learning Using Image Patches. *Investigative Opthalmology & Visual Science* 59(1): 590.

Li, M., Jiang, Y., Zhang, Y. & Zhu, H. 2023. Medical image analysis using deep learning algorithms. *Frontiers in Public Health* 11.

Li, P., Deng, Q. & Li, H. 2020. The Arteriovenous Classification in Retinal Images by U-net and Tracking Algorithm. *2020 IEEE 5th International Conference on Image, Vision and Computing (ICIVC)*, pp. 182–187.

Li, Y., Xia, X. & Paulus, Y.M. 2018. Advances in Retinal Optical Imaging. *Photonics* 5(2): 9.

Marco A. Zarbin. 2012. Diseases of the Retina and Macula. http://njms2.njms.rutgers.edu/eyeweb/casemon/case0299/case0299a.html [17 April 2025].

Nanegrungsunk, O., Patikulsila, D. & Sadda, S.R. 2022. Ophthalmic imaging in diabetic retinopathy: A review. *Clinical & Experimental Ophthalmology* 50(9): 1082–1096.

Nasiruddin, Z.H., Diyana W Zaki, W.M., Assyareefah Hudaibah, S. & Nur Asyiqin, A.H. 2022. Automated Retinal Blood Vessel Feature Extraction in Digital Fundus Images. *4th IEEE International Conference on Artificial Intelligence in Engineering and Technology, IICAIET 2022*, .

Parr, J.C. & Spears, G.F.S. 1974. Mathematic relationships between the width of a retinal artery and the widths of its branches. *American Journal of Ophthalmology* 77(4): 478–483.

Pérez, M.A., Bruce, B.B., Newman, N.J. & Biousse, V. 2012. The Use of Retinal Photography in Nonophthalmic Settings and Its Potential for Neurology. *The Neurologist* 18(6): 350–355.

Riazi Esfahani, P., Reddy, A.J., Thomas, J., Sommer, D.A., Nguyen, A., Farasat, V., Nawathey, N., Bachir, A., Brahmbhatt, T. & Patel, R. 2023. An Analysis of the Usage of Retinal Imaging Technology in the Detection of Age-Related Macular Degeneration. *Cureus*.

Sarao, V., Veritti, D., Borrelli, E., Sadda, S.V.R., Poletti, E. & Lanzetta, P. 2019. A comparison between a white LED confocal imaging system and a conventional flash fundus camera using chromaticity analysis. *BMC Ophthalmology* 19(1): 231.

Sharma, A., Shinde, S., Shaikh, I.I., Vyas, M. & Rani, S. 2021. Machine Learning Approach for Detection of Diabetic Retinopathy with Improved Pre-Processing. *2021 International Conference on Computing, Communication, and Intelligent Systems (ICCCIS)*, pp. 517–522.

Sorrentino, F.S., Jurman, G., De Nadai, K., Campa, C., Furlanello, C. & Parmeggiani, F. 2020. Application of Artificial Intelligence in Targeting Retinal Diseases. *Current Drug Targets* 21(12): 1208–1215.

Staal, J., Abramoff, M.D., Niemeijer, M., Viergever, M.A. & van Ginneken, B. 2004. Ridge-Based Vessel Segmentation in Color Images of the Retina. *IEEE Transactions on Medical Imaging* 23(4): 501–509.

Vázquez, S.G., Cancela, B., Barreira, N., Penedo, M.G., Rodríguez-Blanco, M., Pena Seijo, M., de Tuero, G.C., Barceló, M.A. & Saez, M. 2013. Improving retinal artery and vein classification by means of a minimal path approach. *Machine Vision and Applications* 24(5): 919–930.

Veena, H.N., Muruganandham, A. & Senthil Kumaran, T. 2022. A novel optic disc and optic cup segmentation technique to diagnose glaucoma using deep learning convolutional neural network over retinal fundus images. *Journal of King Saud University - Computer and Information Sciences* 34(8): 6187–6198.

Yan, Z., Yang, X. & Cheng, K.-T. 2018. Joint Segment-Level and Pixel-Wise Losses for Deep Learning Based Retinal Vessel Segmentation. *IEEE Transactions on Biomedical Engineering* 65(9): 1912–1923.

Yang, R. & Qin, J. 2023. Unsupervised Low Illumination Enhancement Model Based on YCbCr Color Space. *2023 8th International Conference on Intelligent Informatics and Biomedical Sciences (ICIIBMS)*, pp. 80–86.

Zhao, Y., Xu, Y. & Wang, T. 2023. Image Segmentation Method Based on Grabcut and Hue-Saturation-Value Color Space Model. , pp. 911–918.

Zhou, M., Jin, K., Wang, S., Ye, J. & Qian, D. 2018. Color Retinal Image Enhancement Based on Luminosity and Contrast Adjustment. *IEEE Transactions on Biomedical Engineering* 65(3): 521–527.

Zubair, M., Umair, M., Ali Naqvi, R., Hussain, D., Owais, M. & Werghi, N. 2023. A comprehensive computer-aided system for an early-stage diagnosis and classification of diabetic macular edema. *Journal of King Saud University - Computer and Information Sciences* 35(8): 101719.